Physics of Fluids

RESEARCH ARTICLE | SEPTEMBER 13 2024

A new design of electro-conjugate fluid micropumps with Venturi and teardrop-shaped electrodes

The Khanh Lai ; Toan Dinh; Minh Duc Nguyen; Ich Long Ngo

Check for updates

Physics of Fluids 36, 092017 (2024)
https://doi.org/10.1063/5.0221203

View Online
Export Citation

Articles You May Be Interested In

Principle and experimental study of a combined teardrop and heart-shaped channel bluffbody valveless piezoelectric pump

Rev. Sci. Instrum. (June 2024)

Experimental and numerical study of the aerodynamic drag crisis phenomenon of a symmetrical thick teardrop airfoil with rounded trailing edge

AIP Conference Proceedings (May 2021)

Bubble-driven inertial micropump

Physics of Fluids (December 2012)

01 October 2024 08:38:07

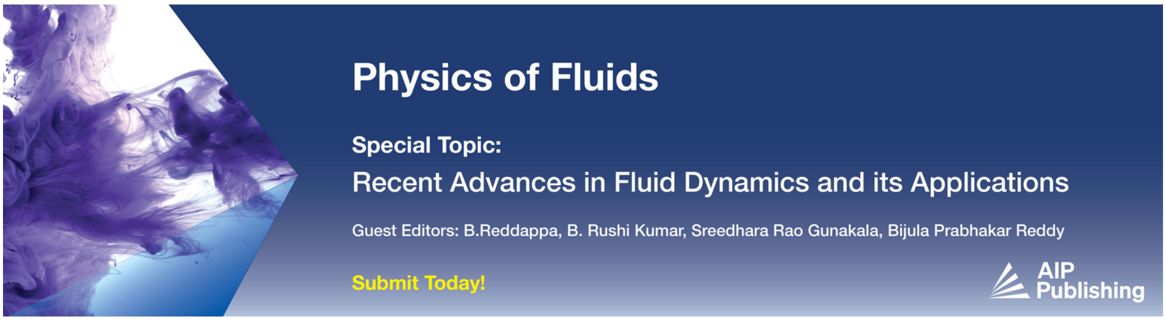

Physics of Fluids

Special Topic:
Recent Advances in Fluid Dynamics and its Applications

Guest Editors: B.Reddappa, B. Rushi Kumar, Sreedhara Rao Gunakala, Bijula Prabhakar Reddy

Submit Today!

AIP Publishing

AIP Publishing

A new design of electro-conjugate fluid micropumps with Venturi and teardrop-shaped electrodes

Cite as: Phys. Fluids **36**, 092017 (2024); doi: 10.1063/5.0221203
Submitted: 30 May 2024 · Accepted: 24 August 2024 ·
Published Online: 13 September 2024

View Online Export Citation CrossMark

The Khanh Lai,[1] Toan Dinh,[2] Minh Duc Nguyen,[1] and Ich Long Ngo[1,a)]

AFFILIATIONS

[1]School of Mechanical Engineering, HUST, No. 01, Dai Co Viet, Hai Ba Trung, Hanoi, Vietnam
[2]School of Engineering, Centre for Future Materials, University of Southern Queensland, Springfield Campus, QLD 4300, Australia

[a)]**Author to whom correspondence should be addressed:** long.ngoich@hust.edu.vn. **Tel./Fax:** +84-243-869-2984

ABSTRACT

This paper presents a newly designed non-mechanical electro-conjugate fluid (ECF) micropump with a Venturi-shaped collector and teardrop-shaped emitter (VD-ECF micropump). The numerical model using the finite element method was thoroughly validated by comparing it with both experimental data and numerical results. Consequently, the characteristic curves of the VD-ECF micropump are significantly affected by both the emitter angle (θ_1) and the collector angle (θ_2). The effects of these angles on the flow behaviors in a VD-ECF micropump were first explained. Furthermore, the performance characteristic curves were elaborately constructed for various operating conditions. The operating ranges of pressure difference and flow rate of the VD-ECF micropump are extended, and they peak at θ_2 approximately from 25° to 30°. Additionally, the maximum efficiency reaches up to 10%, which is the highest figure recorded to date. The obtained results for the new VD-ECF micropump would significantly contribute to the development of ECF micropumps with precise control. Our work also gives valuable guidelines for designing and manufacturing processes of this type of micropump, which has potential applications in microelectronic cooling systems, micro-actuators, and drug transport mechanisms in medical and biomedical fields.

Published under an exclusive license by AIP Publishing. https://doi.org/10.1063/5.0221203

NOMENCLATURE

c	concentration (mol/m^3)
c_0	reference concentration (mol/m^3)
D_t	distance between anode and cathode (m)
De	Debye number (-)
Di	diffusion coefficient (m^2/s)
E	electric field strength (V/m)
E_s	electrostatic field strength (V/m)
E_{thres}	threshold electric field strength (V/m)
F	Faraday's constant (C/mol)
f	normal stress (N/m^2)
H	width of microchannel (m)
H_c	width between two collectors (m)
H_e	width of emitter (m)
I	electric current (A)
J	current density (A/m^2)
k	thermal conductivity (W/m·K)
k_n	proportional constant at the negative electrode (C/V·m^2)
k_p	proportional constant at the positive electrode (C/V·m^2)
L_c	length of collector (m)
L_e	length of emitter (m)
Mc	mobility number (-)
n	normal vector (N/m^2)
Nu	Nusselt number (-)
p	local pressure (Pa)
Pe	Péclet number (-)
Q	flow rate (m^3/s)
R	universal gas constant (kg·m^2/K·mol·s^2)
Re	Reynolds number (-)
T	temperature (K)
U	mean velocity (m/s)
u	local velocity (m/s)
u_{mi}	Einstein mobility (mol·s/kg)
z	charge number (-)

01 October 2024 08:38:07

Greek symbols

α	correction factor (-)
ε	permittivity (F/m)
ε_0	permittivity of free space (F/m)
ε_r	relative permittivity (-)
η	efficiency (%)
θ_1	angle of anode (°)
θ_2	angle of cathode (°)
κ	proportional constants for injected cation and anion density (-)
λ_D	Debye length (m)
μ	viscosity (Pas)
μ_i	ionic mobility ($m^2/(V{\cdot}s)$)
μ_{iw}	ionic mobility determined by Walden's rule ($m^2/(V{\cdot}s)$)
π	PI number (-)
ρ	mass density (kg/m^3)
ρ_v	space charge density (C/m^3)
σ	conductivity (S/m)
ϕ	electric potential (V)
ϕ_0	reference electric potential (V)
∇	nabla operator (-)

Subscripts and superscripts

c	collector (…)
D	Debye (…)
e	emitter (…)
E	electric (…)
F	fluid (…)
i	index, 1, 2, etc. (…)
in	inlet (…)
M	mean (…)
N	negative (…)
out	outlet (…)
P	positive (…)
r	relative (…)
s	static (…)
t	threshold (…)
0	reference index or constant (…)
$*$	dimensional form (…)

I. INTRODUCTION

Micropumps have received considerable attention in recent years due to their excellent mechanical properties, which offer great applications in areas such as microfluidic actuation on organ chips,[1] microfluidic cell culture,[2] drug delivery in the medical field,[3] biomedical technology,[4] and microelectronic cooling.[5] Based on the actuation principle, micropumps can be classified into mechanical displacement and dynamic. Mechanical displacement micropumps are typically developed utilizing moving parts such as diaphragms (piezoelectric, thermo-pneumatic, pneumatic, and bimetallic types), rotary mechanisms (rotating gear and viscous force designs), and acoustic principles (acoustic standing wave micropump), and fluid displacement (ferrofluid and gas boundary type micropump). Micropump is commonly used in microfluidic systems for precise control and manipulation of small volumes of liquid. Due to using a physical actuator or mechanism to perform the pumping function, noise and vibration are unavoidable during pump operation. On the other hand, dynamic micropumps (magnetohydrodynamic, electrohydrodynamic, electroosmotic, electrowetting, electrochemical, flexural planer wave, bubble, evaporation, and electro-conjugate-fluid type micropump) utilize external energy sources to induce fluid motion within microchannels or chambers. Therefore, dynamic micropumps frequently provide higher flow rates and more consistent discharge than mechanical displacement micropumps. Some of the common operating principles, fabricating methods, advantages, and disadvantages of dynamic micropumps, can be found in the literature.[4,6,7]

Among the dynamic micropumps mentioned above, the micropump using electro-conjugate fluid (ECF) is widely used and is considered a promising device. Because the energy is transferred directly to hydraulic power without a moving part, the noise and vibration of the micropump are low.[8] In addition, ECF micropump allows for the generation of stable and constant fluid flows over pumping time due to the continuous energy supply. Therefore, it can be considered a micropressure source for hydraulic control microsystems[9] and other potential applications.[10,11] An ECF is known as one of the dielectric fluids (or smart/structured fluids) that can generate jetting flow when the applied voltage between two electrodes (order of a kilo voltage) is used, owing to the influence of electrostatic forces on dielectric liquids. The jetting flow can be generated actively and strongly under the influence of non-uniform electric field forces and operating conditions, such as ECF type, shape and size of electrodes, and electrode arrangement. Therefore, the ECF is suitable for use as a hydraulic micromotor[12] and in many modern applications.[13]

Indeed, ECFs are widely used in various fields, such as mechanical engineering, chemical engineering, and biomedical engineering. For example, ECF is used in the control of artificial micro muscle cells,[14] a novel flexible finger,[15] a worm-shaped robot,[16] a liquid rate gyroscope,[17] the cooling system for electronic chips,[18] new microparticle translocation methods in microscopic integrated analysis systems (μTAS),[10] and biological systems in animal implantable drug delivery.[19] In particular, ECF can also be used to create tube-type micropumps, which are of interest to this study. Some flow characteristics in this type of micropump with several types of electrodes have been studied worldwide. For example, by using micro-electromechanical systems (MEMS) technology to fabricate triangular prismatic and slit electrodes, Kim *et al.*[8] fabricated one of these micropumps that achieves a certain performance at the applied voltage of 6 kV. Most recently, another experimental study was conducted to optimize the shape and size of the electrodes.[20] Abe *et al.*[10] simultaneously integrated many ECF micropumps to control the movement of microparticles in a microchannel matrix that can be used for chemical synthesis and cell analysis on a biochip. More recently, Kuroboshi *et al.*[21] studied the behavior of ECF current in micropumps with rectangular electrodes and slits. A theoretical model has been proposed to design electrodes of the same type with higher operating performance.

Nowadays, thanks to the strong development of computer technology, the computational fluid dynamics (CFD) method has been carried out effectively and widely to study microfluid[22] and ECF micropumps. For instance, Mori *et al.*[23] used CFD to consider the effect of the dominant factor in ECF flow. This study used four kinds of ECFs: DBD, FF-1_{EHA2}, FF-101_{EHA2}, and FF-909_{EHA2}. Numerical and experimental results of the flow field are in agreement with those

01 October 2024 08:38:07

obtained from the particle image velocimetry. The numerical simulation combines the Poisson–Boltzmann equation and the Korteweg–Helmholtz (KH) equation to develop an ECF flow model for investigating an electric double layer.[24] Kim *et al.*[25] used finite element method (FEM) in COMSOL Multiphysics software to investigate the Onsager effect of fluid flow in the ECF micropump.

For an ECF micropump, as mentioned above, the complex physical phenomenon of the interaction between fluid flow and electric field still needs extensive research.[23] Additionally, ECF micropumps with new designs, higher operating performance, and effective control are also causing some issues in related fields. Based on the literature review, the conventional electrode configurations were considered. For example, needle-ring,[26] square,[27] rectangular (the most common),[21,30] prism-triangular,[10,28] and bullet[25] were used for the emitter, and a slit with an angle of 90° was always used for the collector. However, the micropump efficiency obtained from these configurations is frequently very low (only a few percentages). This means that extremely high electric power is supplied (up to kilowatt), but the output hydraulic power is very low, or the micropump losses are dramatically high. Therefore, a primary innovation introduced in the design of the VD-ECF micropump is to create a new electrode configuration for both the emitter and collector in such a manner that the overall electro-hydraulic efficiency can be improved. Additionally, the operating range of pressure difference and flow rate can also be extended.

This study aims to develop the design and optimization of a new VD-ECF micropump under the influence of many factors, especially the configuration of the electrodes. The FEM was used to solve this problem. Micropump characteristic curves, such as difference pressure–flow rate and efficiency–flow rate, are built to control the ECF micropump thoroughly and comprehensively. Moreover, the electric and hydraulic behaviors in the ECF micropump are observed and fully explained in this research. The numerical results are validated by comparing them with both experimental data and numerical results reported in previous studies. The obtained results are very useful in understanding and developing the ECF micropump.

II. METHODOLOGY

A. Mathematical model

The dynamic behaviors of ECF in the micropump were investigated by using the FEM. Figure 1(a) shows the design of the new micropump, including three pairs of emitter and collector electrodes connected in series. The pressure difference increases, and the operating range of the micropump expands when applied to a series arrangement.[29] The electrode pairs were supplied with applied voltage through two electrode pads (yellow) arranged on both sides. The numerical model and boundary conditions used for the simulation problem are shown in Fig. 1(b) for a pair of electrodes.

In this model, the teardrop-shaped emitter and narrow gap (collector) with dimensions $L_c \times H_c$ are selected as the positive and negative electrodes (grounded, GND), respectively. The sharp angle of the emitter electrode as a function of its thickness is based on the following relationship: $H_e \approx L_e \tan(\theta_1/2)/[0.5 + 0.5\tan(\theta_1/2)]$, where H_e is the thickness of the emitter electrode and L_e is the length of the emitter. When $\theta_2 \neq 90°$, the channel has the shape of a Venturi duct. This term forms the name of the new VD-ECF micropump. ECF flow is generated through adequately high voltage (order of a kilo voltage) application across the anode and cathode and is concentrated mainly at the tail of the anode with θ_1. The flow continues to move and is accelerated through the narrow slit between the two cathodes, generating a jet stream, as illustrated in Fig. 1(b) (yellow arrow). The voltage and electric current values are measured at point B_1, as shown in Fig. 1(b). The ECF micropump characteristics, such as pressure difference–flow rate, are expected to depend on the voltage, electrode configuration, and ECF flow properties, as well as the temperature generated during micropump operation.

Governing equations, which are continuity, momentum, electrostatic, and transport of species, were used to describe the motion of ECF flow under the effects of electric field and advection of generated charges. They are shown in the following equations:

$$\nabla^* \cdot \boldsymbol{u}^* = 0, \tag{1}$$

$$\rho(\boldsymbol{u}^* \cdot \nabla^* \boldsymbol{u}^*) = \nabla^* \cdot \left\{ -p^* \boldsymbol{I} + \mu \left[\nabla^* \boldsymbol{u}^* + (\nabla^* \boldsymbol{u}^*)^{\mathrm{T}} \right] \right\} - F\rho_v^* \boldsymbol{E}^*, \tag{2}$$

$$-\nabla^* \cdot (\varepsilon_0 \varepsilon_r \boldsymbol{E}^*) = F\rho_v^*, \tag{3}$$

$$\nabla^* \cdot \left(\boldsymbol{u}^* c_i^* \right) = \nabla^* \cdot \left\{ D_i \nabla^* c_i^* + \frac{F}{RT_m} D_i z_i c_i^* + \frac{\sigma}{F} \nabla^* \phi^* \right\}, \tag{4}$$

where ρ, μ, $\boldsymbol{u}$, and p are the fluid density, dynamic viscosity, velocity, and pressure, respectively. $\boldsymbol{I}$ is an identity tensor. The last term on the right-hand side of Eq. (2) is electrostatic force acting on the fluid flow under the electric field strength $\boldsymbol{E} = -\nabla\phi$, where ϕ denotes the electric potential. Equation (3) was applied based on Gauss's law, which describes the relationship between charge density and electric field. ε_0 and ε_r in this equation are permittivity constant and relative permittivity, respectively. Space charge density can be defined as a function of the sum of charge number and its concentration, $\rho_v = \sum z_i c_i$. Di, z_i, T_m, R, and F in Eq. (4) stand for diffusion coefficient, charge number, universal constant, mean temperature of testing condition, and Faraday's constant, respectively. These parameters characterize the motion of charges in the fluid flow under the effects of the electric field. The non-dimensional variables are used to solve this problem in a non-dimensional fashion, as shown in the following equation:

$$x = \frac{x^*}{H_c}; \quad y = \frac{y^*}{H_c}; \quad \boldsymbol{u} = \frac{\boldsymbol{u}^*}{U_{in}}; \quad p = \frac{p^*}{\rho U_{in}^2}; \quad c_i = \frac{c_i^*}{c_0}; \quad \phi = \frac{\phi^*}{\phi_0}. \tag{5}$$

In the above-mentioned equation, H_c, U_{in}, c_0, and ϕ_0 are the width of the narrow slit, velocity, concentration, and electric potential, respectively. In summary, Eqs. (1)–(4) can be expressed in a non-dimensional form, as follows:

$$\nabla \cdot \boldsymbol{u} = 0, \tag{6}$$

$$\boldsymbol{u} \cdot \nabla \boldsymbol{u} = \nabla \cdot \left\{ -p\boldsymbol{I} + \frac{1}{\mathrm{Re_F}} \left[\nabla \boldsymbol{u} + (\nabla \boldsymbol{u})^{\mathrm{T}} \right] \right\} + \mathrm{Mc}\rho_v \boldsymbol{E}, \tag{7}$$

$$-\nabla \cdot (\nabla \phi) = \mathrm{De}^2 \rho_v, \tag{8}$$

$$\nabla \cdot \left\{ -\frac{1}{\mathrm{Pe}} \nabla c_i - \frac{\phi_C}{\mathrm{Pe}} z_i c_i \nabla \phi + \boldsymbol{u} c_i - \frac{1}{\mathrm{Re_E}\,\mathrm{De}^2} \nabla \phi \right\} = 0. \tag{9}$$

In the above-mentioned equations, $\mathrm{Re_F}$ is the Reynolds number defined as the ratio of inertial to viscous force. The flow in microchannels is usually laminar; therefore, the value of $\mathrm{Re_F}$ is often small or very

01 October 2024 08:38:07

Published under an exclusive license by AIP Publishing

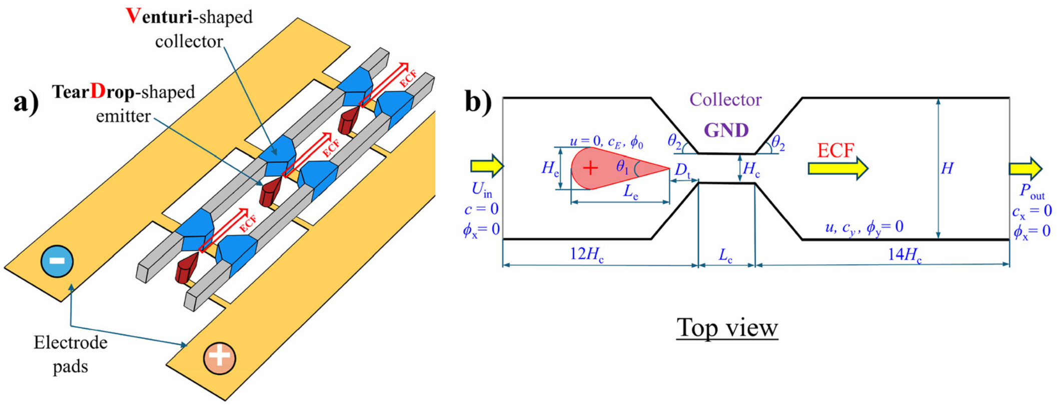

FIG. 1. (a) 3D model of new ECF micropump and (b) schematic of the numerical model and boundary conditions (BC).

small. Mc is a dimensionless number that characterizes the relationship between electric field forces and hydrodynamic forces. This number is expected to influence the flow in the micro-pump significantly. Pe and De are the Peclet and Debye numbers, respectively, where λ_D is the Debye length (a physical quantity used to measure the electrostatic impact of species moving in the solvent). Finally, $\mathrm{Re_E}$ is also the Reynolds number of the electric. The definitions of these important parameters are shown in Eq. (10). The charge distribution around the electrodes can be characterized by these parameters as presented in previous studies,[24,30]

$$\begin{aligned} &\mathrm{Re_F} = \frac{\rho U_{\mathrm{in}} H_{\mathrm{c}}}{\mu}; \quad \mathrm{Mc} = \frac{F c_0 \phi_0}{\rho U_{\mathrm{in}}^2}; \quad \mathrm{Pe} = \frac{U_{\mathrm{in}} H_{\mathrm{c}}}{D_{\mathrm{i}}}; \quad \phi_{\mathrm{C}} = \frac{F\phi_0}{R T_{\mathrm{m}}}; \\ &\mathrm{De} = \frac{H_{\mathrm{c}}}{\lambda_D} \ \text{ where } \lambda_{\mathrm{D}}^2 = \frac{\varepsilon_0 \varepsilon_{\mathrm{r}} \phi_0}{F c_0}; \quad \mathrm{Re_E} = \frac{\varepsilon U_{\mathrm{in}}}{\sigma H_{\mathrm{c}}}; \quad \mathrm{Nu_E} = \frac{k_{\mathrm{p}}^* \phi_0}{F c_0 H_{\mathrm{c}}}. \end{aligned} \tag{10}$$

The BC used for this problem is also shown in Fig. 1(b). To model the emission of species from the electrodes, the BC as a function of charge concentration is used, as shown in Eq. (10),[28] expressed in a dimensionless form, where E_{S} and E_{thres} correspond to the electrostatic and threshold field strength, respectively. When $E_{\mathrm{S}} \geq E_{\mathrm{thres}},$ the charge is emitted or collected from the electrode, and vice versa when $E_{\mathrm{S}} < E_{\mathrm{thres}}$. In addition, α in Eq. (11), the correction factor takes into account measurement errors and discrepancies between experiment and numerical simulation results. $\kappa = k_{\mathrm{n}}{}^{*}/k_{\mathrm{p}}{}^{*}$ are proportional constants for injected cation (positive) and anion (negative) density. These parameters and E_{thres} are frequently determined by experiments and influenced by testing temperature.[31,32] $\mathrm{Nu_E}$ parameters were mentioned above in Eq. (10). Finally, the function $\mathrm{sign}(\phi)$ indicates the sign of the expression according to the value of the electric potential ϕ_0 corresponding to the case of emitting or collecting charge,

$$c_{\mathrm{E}} = \alpha \mathrm{Nu_E} (E_{\mathrm{S}} - E_{\mathrm{thresP}}) \mathrm{sign}(\phi_0)$$

and

$$c_{\mathrm{N}} = \kappa \alpha \mathrm{Nu_E} (E_{\mathrm{S}} - E_{\mathrm{thresN}}) \mathrm{sign}(\phi_0). \tag{11}$$

B. Code validation

We validate the numerical model presented in Sec. II A by comparing it with the experimental and simulational results obtained by Tran *et al.*[31] and Nishikawara *et al.*[33] Figures 2(a) and 2(b) show the results with the same operation conditions, $\phi_0 = -10\,\mathrm{kV}$, the distance between anode and cathode $s = 5\,\mathrm{mm}$, and the temperature $T_{\mathrm{m}} = 313$ K. Figures 2(a) and 2(b) also show the vortex of an experiment by Tran *et al.*[31] and the simulation by the present work, respectively. The location of the vortex center and the intensity are slightly different, which may be due to the following reasons: (i) only one type of ion is assumed to exist in this case, (ii) differences in determining the parameters k_{p}, k_{n}, and E_{thres} from experiments,[31,32] (iii) the uneven distribution and residence of species when moving at the electrodes, and (iv) the effect of temperature due to high voltage during experiments (in the order of a kilo voltage).

However, both results are similar and suitable for the tendency of vortex formation and development. Figure 2(c) shows the quantitative demonstration, with the average velocity determined in a square region with dimensions $1\,\mathrm{mm} \times 1\,\mathrm{mm}$. The applied voltage ϕ_0 is changed from 7 to 15 kV. Figure 3(c) shows that the numerical simulation results agree with the experimental results in both tendency and magnitude. Furthermore, our study yields results that are closer to the experimental data than previous numerical simulations, as shown in Fig. 2(c) (red lines vs blue lines and square points). This is correct for all three correction factor values $\alpha = 1$, 1.1, and 1.2 considered. The maximum deviation is less than 9% compared to the experimental data for $\alpha = 1.1$. Therefore, $\alpha = 1.1$ is used for further calculations in this study.

In addition, the study also conducted other validation results. Notably, the results are comparable to those of Nishikawara *et al.*[33] Because the authors also aim to study the electro-hydraulic flow in a micropump using ECF, the results are expected to be more reliable and more suitable for practical application. Qualitative and quantitative results are shown in Figs. 3 and 4, respectively. The distribution field of the concentration [Fig. 3(b)] of the present work compared with the results of Nishikawara *et al.*[33] [Fig. 3(a)] shows that the concentration distribution from the two studies is similar in both tendency and value range. However, there are still some differences; for example, the region of the highest charge concentration directed from the positive electrode to the negative electrode is more concentrated in the present work. This is due to errors in the choice of mesh model, adaptive mesh (present work), and uniform mesh (Nishikawara *et al.*[33]). Both results generally agree with each other, and this predicts matching results, as shown quantitatively in Fig. 4.

01 October 2024 08:38:07

Published under an exclusive license by AIP Publishing

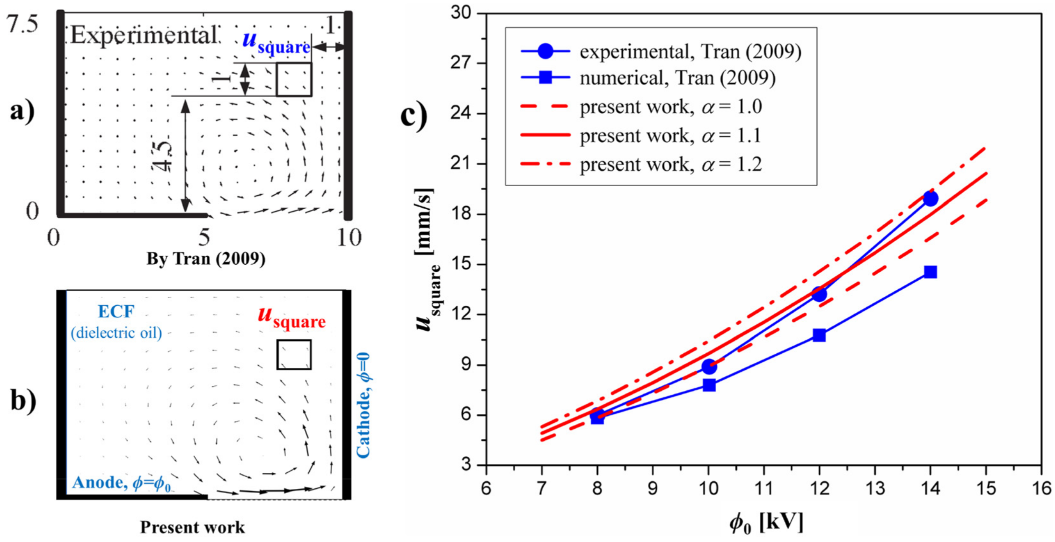

FIG. 2. Model evaluation results compared with experimental results by Tran *et al.*[31]: (a) and (b) velocity vector field, $\phi_0 = -10$ kV, and (c) average velocity in the square according to the applied voltage, with $s = 5$ mm and $T_m = 313$ K.

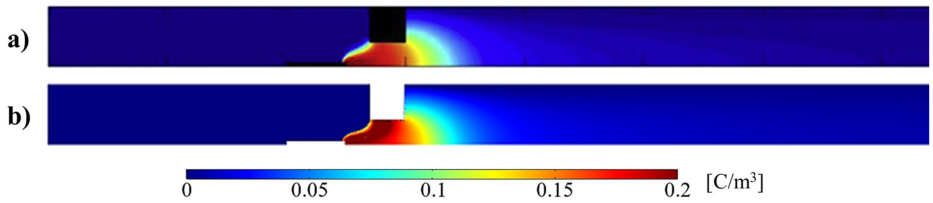

FIG. 3. The distribution of concentration field (a) Nishikawara *et al.*[33] and (b) present work for $\phi_0 = 5$ kV and $Q = 0.1$ cm^3/s.

Indeed, the quantitative results shown in Fig. 4 show a good agreement between the two results. The flow range is selected from 0 to 0.15 cm^3/s. The pressure difference was determined at the micropump's inlet and outlet. When increasing the length of the electrode (L), pressure difference (Δp) continues to increase when the flow rate is at small values, flow rate $Q = 0$ and 0.05 cm^3/s. However, this trend changes for higher Q values. Specifically, Δp increases as L increases from 0.15 to 0.3 mm; it reaches a maximum at $L = 0.3$ mm and then decreases with further L increase, as shown in Fig. 5 for $Q = 0.1$ and 0.15 cm^3/s. This trend is actual for both results. Additionally, the maximum deviation is shown to be less than 5%. Therefore, once again, the numerical model has been evaluated extensively and can be widely applied to calculate numerical simulations for investigated novel micropumps.

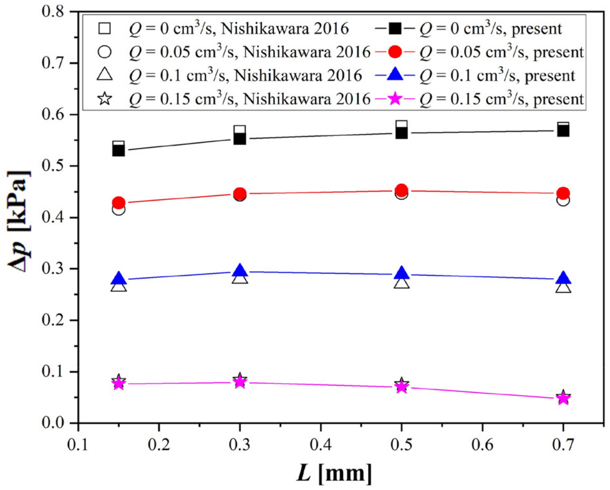

FIG. 4. Pressure difference Δp as a function of the length of electrode[33] for $\phi_0 = 5$ kV.

The adaptive mesh refinement (AMR) has been used to guarantee grid convergence and is a very sensitive aspect of this multi-physic problem. This approach dynamically refines the mesh based on the solution's local error, allowing for a more accurate representation of the physics within the computational domain. The AMR process starts with an initial coarse mesh and iteratively refines it in regions where the solution exhibits significant variations or gradients. This refinement continues until the desired level of accuracy is achieved or a specified stopping criterion is met. In particular, the maximum number of refinements and adaptions is 5 and 2, respectively. The critical advantage of AMR is its ability to allocate computational resources more efficiently by concentrating grid points in areas where they are most needed, such as near boundaries, interfaces, or regions with sharp gradients. This adaptive refinement strategy not only improves the accuracy of the solution but also reduces computational costs by

01 October 2024 08:38:07

Published under an exclusive license by AIP Publishing

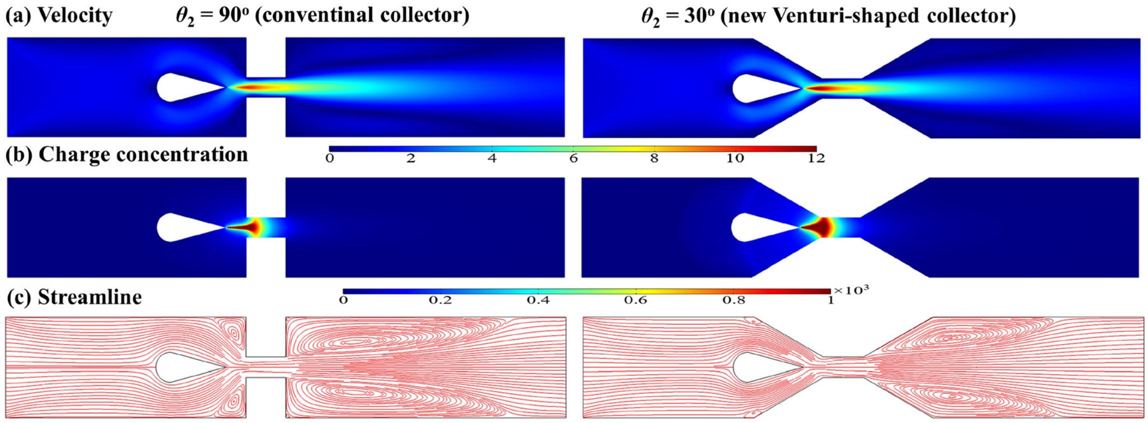

FIG. 5. Distribution of (a) velocity field, (b) charge concentration field, and (c) streamline for conventional and new Venturi-shaped collector, for $\theta_1 = 30°$, $\phi_0 = 6$ kV, and $Q = 400$ ml/h.

minimizing the number of grid points required to achieve the desired level of accuracy. In addition, details about grid convergence in ECF micropumps have been mentioned in a previous research work.[34]

III. RESULTS AND DISCUSSIONS

A. Effects of Venturi-shaped collector

In previous studies, the design of ECF micropump primarily focused on emitters, such as needle-ring,[26] square,[27] and rectangular.[21,32] However, to the best of our knowledge, no research has considered the effect of collectors in the ECF micropump. Therefore, this study proposes a new design with the innovative Venturi-shaped collector and teardrop-shaped emitter of the ECF micropump. The design of the Venturi duct is predicted to minimize hydraulic loss by generating a suction region in the narrow segment of the channel and mitigating vortex losses.[35,36] Traditional ECF micropumps control differential pressure (Δp), flow rate (Q), and efficiency solely by adjusting the applied voltage. However, the VD-ECF micropump introduces an additional feature: the ability to adjust the angles of the emitter (θ_1) and collector (θ_2). This allows for more precise control over these parameters. Indeed, Fig. 5 shows the qualitative simulation results of the ECF flow through the micropump under various values of θ_2 for $\theta_1 = 30°$, applied voltage $\phi_0 = 6\,\text{kV}$, and $Q = 400\,\text{ml/h}$. The velocity, charge concentration, and streamline distributions are shown in Figs. 5(a)–5(c), respectively, for two particular cases, the conventional collector ($\theta_2 = 90°$, left), and the new Venturi-shaped ($\theta_1 = 30°$, right). More information about the distribution of velocity, charge concentration, and streamline for Venturi-shaped collector shape ($\theta_2 = 45°$ and $\theta_2 = 60°$) is included in Fig. 17. It was found that the behavior of ECF flow in the micropump significantly depends on the collector shape. The velocity distribution regions between the emitter and collectors become narrow [Fig. 5(a)], and the regions with high charge concentration are expanded [Fig. 5(b)] when decreasing θ_2. It may imply that a stronger flow can be generated with a smaller θ_2 under the same operating conditions.

In addition, vortices can form when fluid flows through ECF micropumps,[27] especially when there are changes in flow velocity, direction, or obstacles (electrodes). These vortices are essentially swirling motions of the fluid that disrupt the smooth flow and can lead to various issues: (i) energy loss, (ii) increased friction, and (iii) noise and vibrations. Therefore, the decrease in θ_2 may reduce the vortex region between the emitting and collecting electrodes;[32] hence, hydraulic losses can be reduced in the VD-ECF micropump. Indeed, as shown in Fig. 5(c) (left), the vortices appear in both regions in front and behind the collector. When decreasing θ_2, the vortices in these regions tend to shrink, and the front vortex region narrows faster, as shown in Fig. 5(c) (right). This is a basic idea in this new micropump design. Therefore, the new thermo-hydrodynamic characteristics of the VD-ECF micropump are expected to be gained.

Indeed, Fig. 6(a) shows quantitative results of the pressure difference (Δp)–flow rate (Q) characteristics for various values of θ_2 ranging from 15° to 90°. Figure 6(a) indicates that Δp-Q curves tend to expand the operating range of both pressure difference and flow rate when decreasing θ_2 to around 30°. However, the operating range becomes narrow when θ_2 decreases to 15°. Notably, $\theta_2 = 30°$ is the smallest opening angle achieved for the collector in the ECF micropump, as reported in the literature,[33] but in this study, the range of θ_2 expanded to 15°, as shown by the black dash-dot in Fig. 6(a). The trend of Fig. 6(a) is also valid for other values of the applied voltages, as shown in Fig. 6(b). To find more effects of the collector angle θ_2, the flow rate of ECF micropump is fixed $Q = 200\,\text{ml/h}$, and the pressure difference is calculated at three applied voltage values of $\phi_0 = 4$, 6, and 8 kV, as shown in Fig. 6(b). Consequently, the maximum deviation of the pressure difference is 52.3%, 31.6%, and 26.2% at $\phi_0 = 4$, 6, and 8 kV, respectively. Therefore, it is predicted that an optimal value of the collector angle exists at which the maximum pressure difference of the micropump reaches. This result is very useful in optimizing the actual operating range of the pump and controlling the pump according to design requirements.

In addition to the effects of collector angle and channel geometry on the hydrodynamic aspect, θ_2 is also predicted to affect the distribution and electrokinetic behavior in the ECF micropump. Figure 7(a) illustrates the quantitative relationship between the electric field and variation along the centerline of the ECF micropump for various values of θ_2, with $\theta_1 = 30°$ and $\phi_0 = 4\,\text{kV}$. Initially, the magnitude of the electric field (E) is generally constant from the inlet to the emitter. However, it tends to increase slightly at C_1, where the maximum thickness of the emitter exists. Then, E reaches its extreme value near the tip of the emitter (point C_2); this conclusion is consistent with the results

01 October 2024 08:38:07

Published under an exclusive license by AIP Publishing

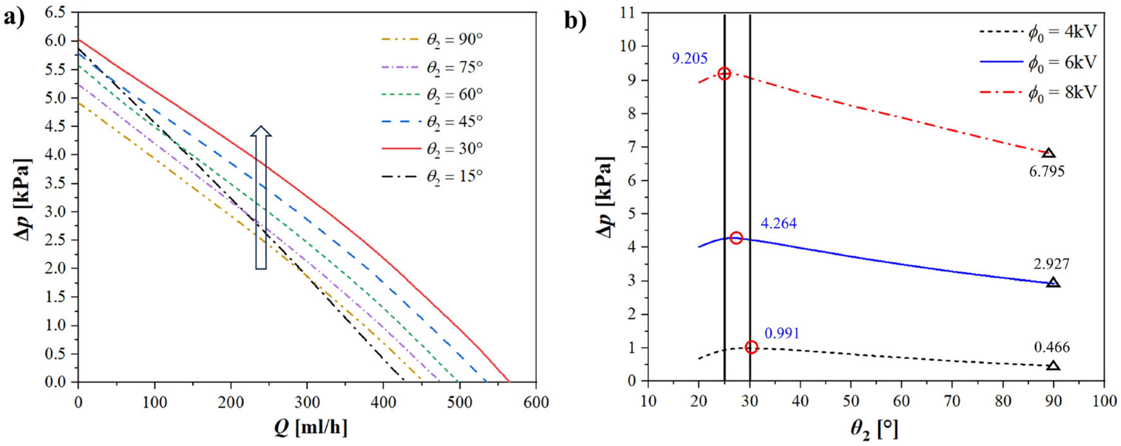

FIG. 6. Effect of θ_2 on (a) the characteristic curves Δp-Q, for $\phi_0 = 6$ kV, and (b) pressure difference as a function of θ_2, for $\theta_1 = 30°$ and $Q = 200$ ml/h.

from the literature.[26] From point C_2 to C_3, the electric field intensity decreases rapidly. The electric field is maximal at $\theta_2 = 15°$ and minimal at $\theta_2 = 90°$. This is because when θ_2 decreases, the distance between two electrodes becomes relatively shorter. The electric field is inversely proportional to the square of the distance between the emitter and collector, as described by Coulomb's law for electrostatic. Therefore, it implies that E will become larger as θ_2 becomes smaller. However, the trend of the variation from point C_3 to the output of the ECF micropump reversed. Specifically, the electric field of $\theta_2 = 90°$ is the highest, and $\theta_2 = 15°$ is the lowest, as shown in Fig. 7(a). In addition, Fig. 7(b) shows that the distribution of charge density (ρ_v) is similar to the above-mentioned trend for E [Fig. 7(a)], even the variation in magnitude at C_3. Indeed, the electric field is linearly proportional to the charge density, as shown by Eq. (3).

To examine more effects of θ_2 on the performance of ECF micropump, electric field and charge density values are measured averagely on the domain, and electric current (I) is calculated on the collector surface, as shown in Fig. 8(a). This figure shows that when θ_2 decreases, all three values of ρ_v, E, and I increase. In addition, when the electric field increases, the current density (J) increases. Furthermore, I is the integration of current density over the electrode area yielding the total current. Therefore, I increase as E increases or θ_2 decreases. The maximum deviations between $\theta_2 = 15°$ and $\theta_2 = 90°$ are 233.3%, 157.7%, and 623.2% for the three values of ρ_v, E, and I, respectively. Figure 8(b) illustrates the electric power (N_e), hydraulic power (N_p), and efficiency (η) for various values of θ_2 for $\theta_1 = 30°$, $\phi_0 = 4$ kV, and $Q = 100$ ml/h. Additionally, the increase in ρ_v and E may cause the increase in N_p. This is because the dominant force in the ECF micropump is the Coulomb force.[27] This force interacts with other forces to result in the existence of maximum hydraulic power, as shown in Fig. 8(b) (N_p-θ_2 line). Moreover, it was found in previous literature[21] that when the distance between the emitter and collector becomes shorter, the hydraulic power may increase. However, the increase in N_p (0.4%) is much smaller than the increase in N_e (623.3%). Therefore, it implies that the ECF micropump efficiency decreases with decreasing θ_2 since the efficiency is a function of hydraulic power (pressure difference and flow rate) per electric power consumption (applied voltage and electric current), as shown in Eq. (12). In summary, although the efficiency of the VD-ECF micropump with smaller collector angle tentatively decreases compared to the conventional micropump ($\theta_2 = 90°$), the maximum hydraulic power can be reached at an optimized θ_2,

$$\eta = \frac{\Delta p Q}{\phi_0 I}. \tag{12}$$

Figure 9 depicts a visualization of the conclusions mentioned previously. The impact of θ_2 on the electrokinetic becomes evident, especially in the region between two electrodes. At $\theta_2 = 90°$, E is mainly concentrated at the emitter's tip and the collector's right-angle apex because this point is closest to the emitter. Then, when θ_2 decreases, E becomes more concentrated (the red region) in the narrow gap between the emitter and collector. The maximum electric field strength also increases accordingly, i.e., 29.19, 33.03, 40.06, and 46.25 for $\theta_2 =$ 90°, 60°, 30°, and 15°, respectively. This means that the dynamic behavior of the electrokinetic flow in the new design of the ECF micropump is remarkably affected by the collector angle.

In addition, Fig. 10 shows the characteristic curves of the ECF micropump under specific operating conditions ($\theta_1 = 30$, $\theta_2 = 60°$, and $\phi_0 = 6$ kV). The pressure difference–flow characteristic curve typically takes the form of negative linearity, indicating a decrease in the pressure difference of the micropump as the flow rate increases. The relationship between hydraulic power and flow rate often resembles that between efficiency and flow rate. The hydraulic power and efficiency of the micropump typically increase with the flow rate and reach a maximum value at the ideal operating point before decreasing as the flow rate continues to increase.

This operating point is called the design point, where the micropump achieves maximum efficiency and power output. Notably, the actual operating flow rate range may vary by up to ±5% without affecting the efficiency, as illustrated in Fig. 10. Additionally, Figs. 18 and 19 show the design points under varying operating conditions with the various values of ϕ_0. This expands the possibilities for multiple operating points to obtain the performance characteristic curves, as shown in Fig. 11. Performance efficiency maps are constructed by varying θ_2 from 15° to 90° and ϕ_0 ranging from 2 to 10 kV and

01 October 2024 08:38:07

Published under an exclusive license by AIP Publishing

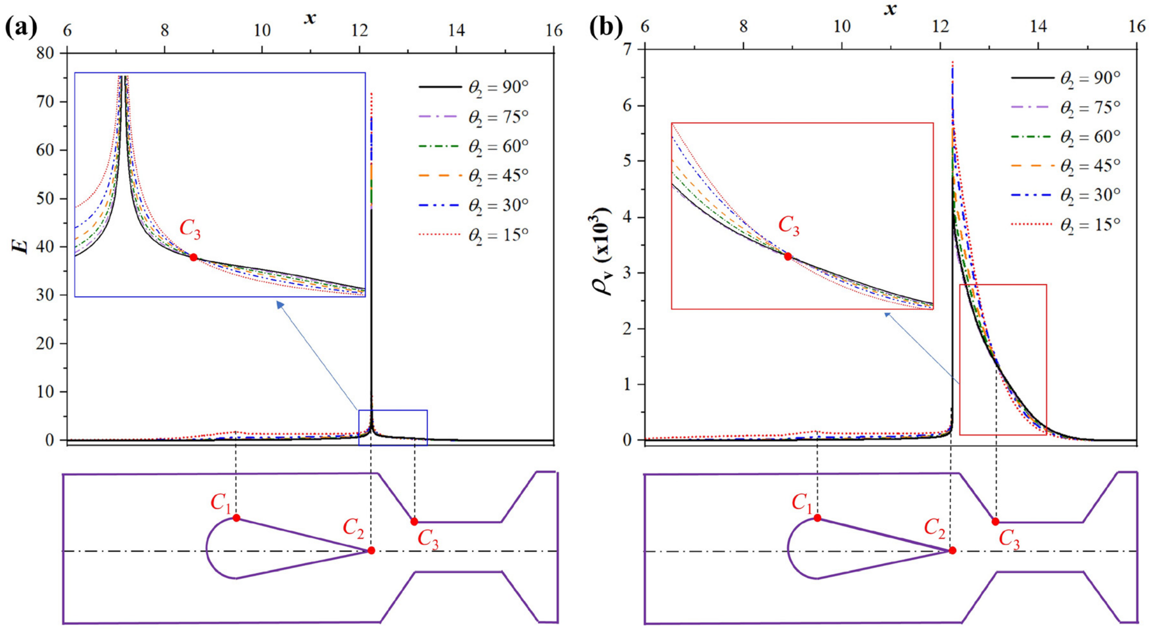

FIG. 7. (a) Electric field and (b) charge density variation along the centerline for various values of θ_2 for $\theta_1 = 30°$ and $\phi_0 = 4$ kV.

connecting the design points. Figure 11 illustrates the efficiency–flow rate characteristics curve for various θ_2 and ϕ_0 with $\theta_1 = 30°$ [Fig. 11(a)] and $\theta_1 = 60°$ [Fig. 11(b)].

In general, when maintaining the applied voltage constant, the maximum efficiency increases when θ_2 increases. Moreover, the results showed that the stronger applied voltages resulted in a higher maximum efficiency, thereby causing the ECF micropump's higher flow rates, meaning maximum efficiency increases within a larger flow rate range. This was because high applied voltages could generate high volume force, which enhanced the efficiency. The maximum efficiency is achieved at higher flow rate points when θ_2 is between 15° and 30°. However, this trend changes, meaning the maximum efficiency is achieved at lower flow rate points when θ_2 is between 30° and 90°, as shown in Fig. 11(a). This indicates that the maximum efficiency is achieved within the widest flow rate range when the angle θ_2 has an optimal value (e.g., $\theta_2 = 30°$). Additionally, both the maximum efficiency and flow rate ranges decrease as θ_1 increases, which will be further explained in Sec. III B, the effect of the teardrop-shaped emitter. Therefore, it can be concluded that for applications requiring a wide range of pressure and flow rates, $\theta_2 = 30°$ is recommended, whereas, for efficiency considerations, $\theta_2 = 90°$ should be utilized.

Finally, this section presents a comprehensive study of the influence of the collectors and channel geometry through θ_2. The results regarding the hydrodynamic and electrokinetic behavior of the

01 October 2024 08:38:07

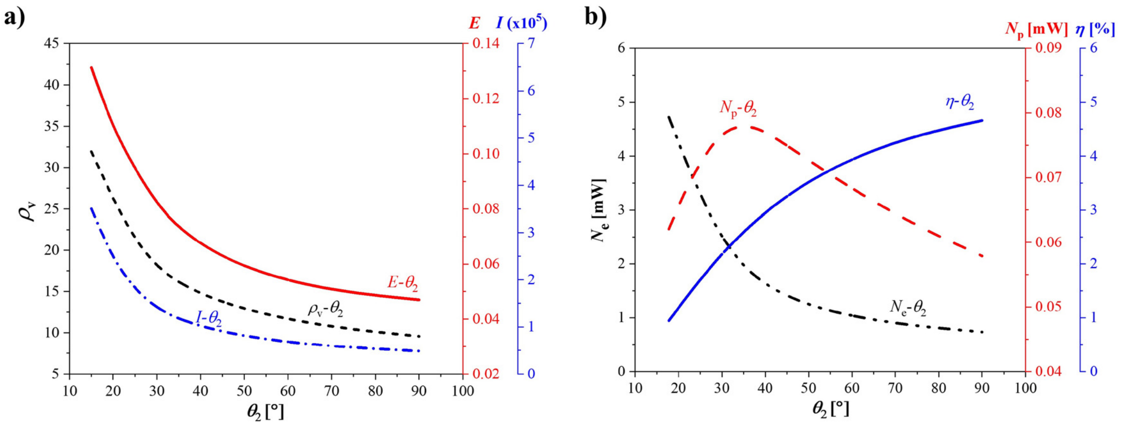

FIG. 8. (a) Charge density, electric field, and electric current for various values of θ_2, and (b) electric power, hydraulic power, and efficiency for various values of θ_2 for $\theta_1 = 30°$, $\phi_0 = 4$ kV, $Q = 100$ ml/h.

Published under an exclusive license by AIP Publishing

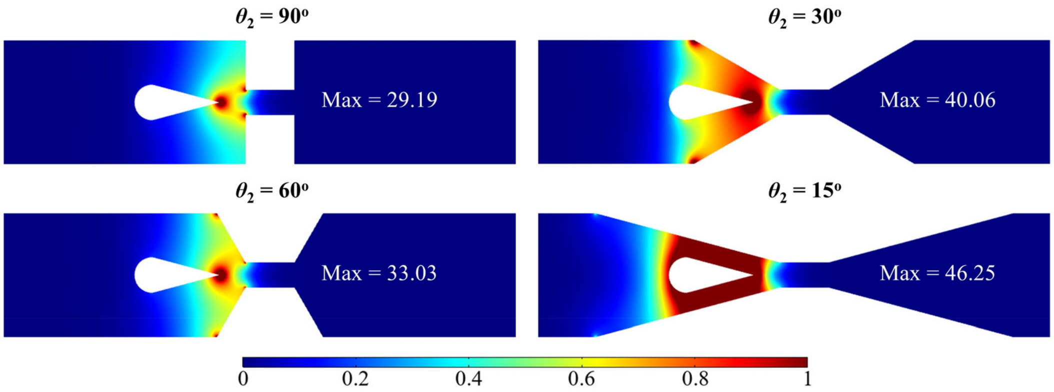

FIG. 9. Distribution of electric field for various values of θ_2 for $\theta_1 = 30°$ and $\phi_0 = 4$ kV.

VD-ECF micropump have been thoroughly investigated, both qualitatively and quantitatively. Based on the results from Figs. 6(b), 11, and 18, the pressure difference and flow rate of the ECF micropump reach the maximum at θ_2 approximately from 25° to 30°. This represents a novel design point identified in this study.

B. Effects of teardrop-shaped emitter

The varying shapes of the emitter significantly impact the dynamic behavior of the fluid flow in the ECF micropump.[37] Therefore, numerous studies on the geometric shapes of the emitter in the ECF micropump, such as needle-ring,[26] square,[27] and rectangular,[21,32] (the most common) were studied extensively in the first phase. Then, other shapes, such as prism-triangular[10,28] and bullet,[25] are continuously investigated and developed. In comparison with needle-ring and square electrodes, prism-triangular and bullet electrodes are extensively utilized owing to their elevated output power density and compatibility with MEMS processes.[38] Because the charge is actively emitted from the sharp tip of the positive electrode, it can affect the operational characteristics.[37] Thus, the acute angle of the emitter θ_1 is necessary to examine. Therefore, this study proposes a novel teardrop-shaped emitter that offers good hydrodynamic properties, promoting smooth and uninterrupted flow, uniformity, and reduced resistance, particularly in narrow channels.[35,36] Additionally, it consistently maintains a sharp tail angle compared to other electrodes. Consequently, the thickness and region of the teardrop-shaped emitter, bullet, and prism-triangular electrode shapes were kept constant for comparison purposes.

The characteristic curves Δp-Q and η-Q are shown in Figs. 12(a) and 12(b), respectively, with operation conditions $\theta_2 = 90°$ and $\phi_0 = 2$ kV. This figure indicates that Δp-Q generated by the tear droplet profile (red solid line) has the largest value among the three electrode shapes outlined above. The increase in Δp for the tear droplet profile is up to 37.1% and 56.1% compared with that of the bullet and the prism-triangular for $\phi_0 = 2$ kV and 52.7% and 65.1% for $\phi_0 = 4$ kV, respectively. With the results shown in Fig. 12(b), the utilization of the tear droplet profile is anticipated to enhance the electrohydraulic efficiency of the ECF micropump. Indeed, when comparing tear droplet profiles with other conventional electrodes, there is a significant increase in efficiency η. Practically, $\phi_0 = 2$ kV demonstrates a rise in the efficiency of up to 20.1% and 29.9%, respectively. For $\phi_0 = 4$ kV, the efficiency reaches up to 36.5% and 45.8%; all comparisons are measured at the design point shown in Fig. 10. Moreover, the results obtained from Fig. 12 also indicated that the operating range of pressure difference and flow rate is extended using the teardrop-shaped electrode compared to conventional electrodes. The primary emphasis of this study lies in the novel design of the teardrop-shaped emitter. These results demonstrated the potential efficacy of the new teardrop-shaped emitter designed for the VD-ECF micropump.

Figure 13 shows the velocity and charge concentration distribution in the VD-ECF micropump for various values of θ_1 ranging from 15° to 75°. When θ_1 becomes smaller, the flow velocity when entering the narrow gap region increases [Fig. 13(a)]. In addition, the charge concentration behind the tip of the emitter is the same trend with velocity. Indeed, when θ_1 is decreased, θ_1 becomes sharper, leading to a higher electric field intensity that could generate more powerful ECF jetting.[39]

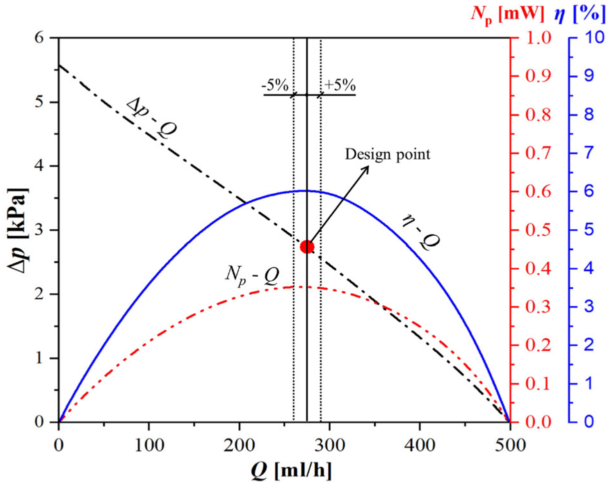

FIG. 10. Characteristic curves and design point of the VD-ECF micropump for $\theta_1 = 30°$, $\theta_2 = 60°$, and $\phi_0 = 6$ kV.

01 October 2024 08:38:07

Published under an exclusive license by AIP Publishing

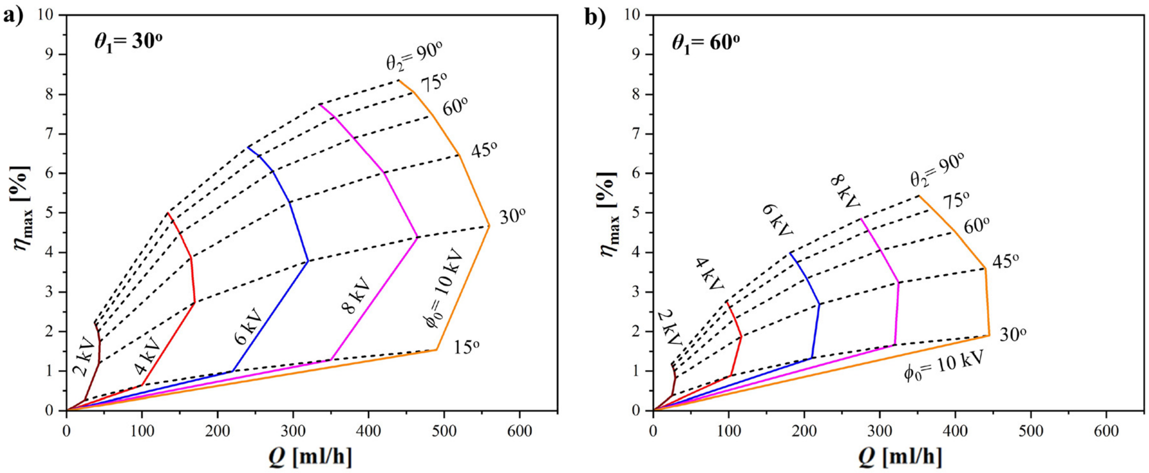

FIG. 11. The performance characteristic curves of VD-ECF micropump for various θ_2 and ϕ_0 (a) $\theta_1 = 30°$ and (b) $\theta_1 = 60°$.

For the influence of both emitter and collector angles, the trailing-edge emitter and collector angles influence the flow dynamic behaviors in the VD-ECF micropump, as shown in Figs. 5, 9, and 13. Specifically, when the collector angle is changed from 90° to 30°, the ECF jet flow becomes stronger, and the charge concentration region becomes larger. Additionally, the vortices in the VD-ECF micropump tend to decrease and disappear depending on the specific operating conditions when the collector angle becomes smaller. The electrokinetic behavior is also affected by the collector angle. The maximum value of the electric field increases in the region between the emitter and collector when θ_2 decreases. Similar to the trend of θ_2, the velocity, charge concentration region, and electric field increase when the emitter angle θ_1 decreases.

Figure 14 shows the variation of the drag coefficient (C_D) with θ_1 for various applied voltages [Fig. 14(a)] and various flow rates [Fig. 14(b)]. The drag coefficient is calculated using the drag force combining the pressure and viscous forces acting on the emitter. The results show that the drag coefficient increases with increasing θ_1. Indeed, it implies that the thickness of the emitter increases when θ_1 increases, resulting in greater flow resistance and lower velocity. In addition, when the applied voltage increases, the curve of the drag coefficient C_D is lifted, as shown in Fig. 14(a). However, this trend changes when the flow rate increases, as shown in Fig. 14(b). Notably, an increase in the flow rate corresponds to an increase in the fluid Reynolds number. This conclusion is consistent with the results from the literature for turbulent flow.[40] This similarity highlights the commonality between the two flow regimes. Conversely, the relationship between C_D and Re_F develops in the opposite direction. This is also a distinguishing feature between the two flow regimes. Furthermore, an important result is the significant variation in the drag coefficient at very low Re_F ranges, which typically applies to flow in microchannels in general and in micropumps in particular. The drag coefficient at the largest emitter angle is nearly eight times greater than that at the smallest emitter angle. Therefore, this result is valuable and is anticipated to

01 October 2024 08:38:07

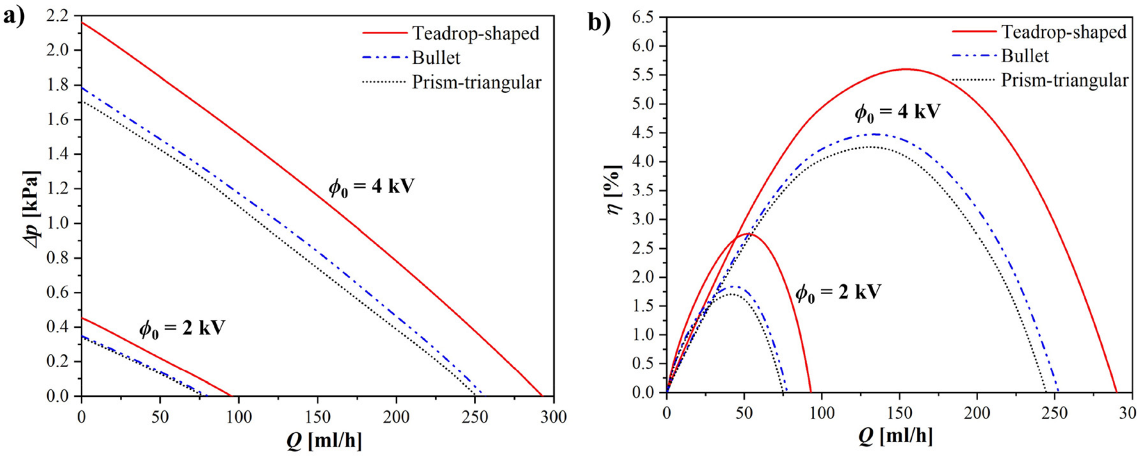

FIG. 12. Comparing characteristic curves of three electrode shapes for (a) Δp-Q and (b) η-Q.

Published under an exclusive license by AIP Publishing

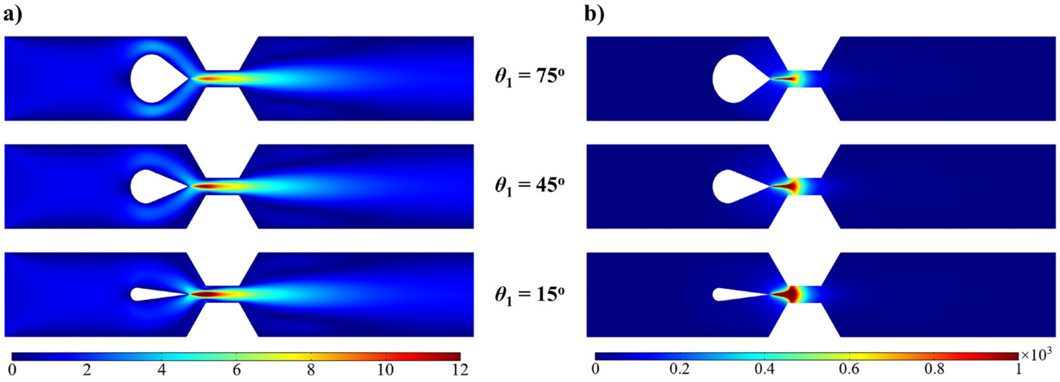

FIG. 13. Distribution of (a) velocity field and (b) charge concentration for various θ_1, with $\theta_2 = 60°$, $\phi_0 = 6$ kV, and $Q = 300$ ml/h.

significantly impact the operation capability and overall performance of the ECF micropump.

Figure 15 shows quantitative results regarding the impact of θ_1 on Δp-Q of the ECF micropump. In Fig. 15(a), the operating range of both pressure difference and flow rate is extended when decreasing θ_1 from 90° to 15°, as shown in Fig. 15(a). The trend is also valid for other applied voltage ranges, as shown in Fig. 15(b). To consider more effects of the emitter angle θ_1, the flow rate is fixed $Q = 100$ ml/h, and the pressure difference is calculated at three applied voltage values, as shown in Fig. 15(b). The points of maximum and minimum pressure difference along the curve for $\phi_0 = 4$ kV is 2.01 and 0.23, respectively, with a maximum deviation of 226.8%. For $\phi_0 = 6$ kV, the maximum and minimum pressure difference points are 5.92 and 1.54, respectively, with a maximum deviation of 282.5%. Finally, for $\phi_0 = 8$ kV, they are 11.53 and 3.52, respectively, with a maximum deviation of 752.6%. The points of maximum pressure difference are marked with circles. In contrast, the points of minimum pressure are marked with triangles, as shown in Fig. 15(b). In addition, the effects of θ_1 on the electrokinetic behavior of the ECF micropump are demonstrated in Fig. 20 (qualitative aspect). The maximum electric field strength increases as θ_1 decreases. Specifically, the values are 14.26, 24.63, 33.03, and 47.79 for $\theta_1 =$ 90°, 60°, 30°, and 15°, respectively. From these results, it can be predicted that the smaller the angle θ_1, the micropump may have a wide operating flow rate range and create a large pressure difference, as explained above. However, from the previous literature for emitter angle,[21] it was found that the deformation of the micro molds and, after the long operating period, the sharp tip edge becomes more severe as the emitter angle becomes smaller ($\theta_1 < 30°$). Therefore, to ensure the feasibility of fabrication and durability of the micropump, $\theta_1 = 30°$ is proposed in this study.

Finally, the performance characteristic curves are depicted in Fig. 16, encompassing maximum efficiency $\eta_{\max}$, flow rate Q, applied voltage ϕ_0, and geometric parameters such as θ_1 and θ_2. During design and manufacturing as well as operation, the initial step in utilizing these characteristic curves involves selecting predetermined configurations, θ_1 and θ_2, and the applied voltage range ϕ_0. Subsequently, the flow rate range required for the ECF micropump is computed. Utilizing the characteristic curves with the applied voltage range ensures that the flow rate range is maximized or the efficiency is optimized to achieve the most energy-efficient operation. Moreover, to compute other points within the range of Q from 0 to 600 ml/h and the applied voltage from 2 to 10 kV, interpolation methods (both linear

01 October 2024 08:38:07

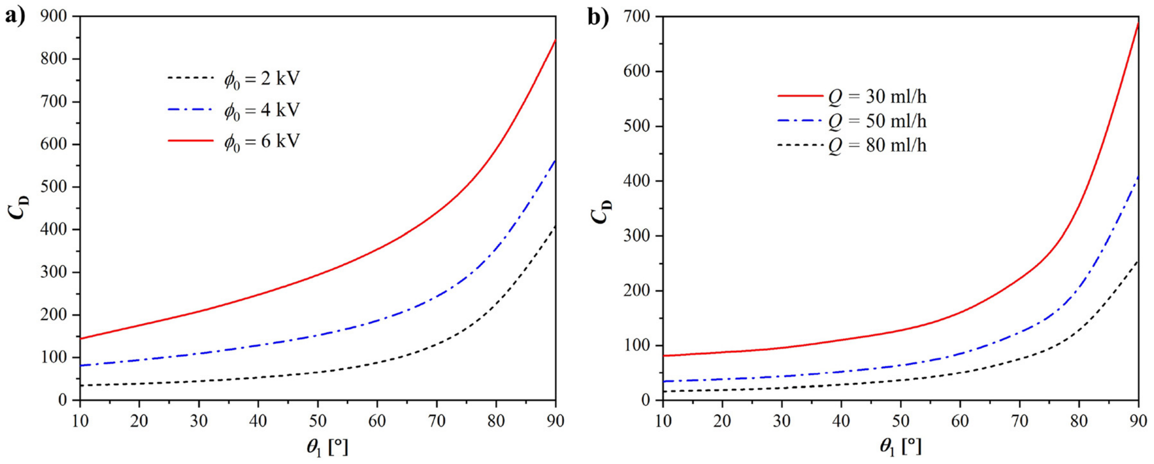

FIG. 14. Drag force coefficient as a function of θ_1 (a) for various values of ϕ_0 with Q= 100 ml/h and (b) for various values of Q with $\theta_2 = 30°$ and $\phi_0 = 4$ kV.

Published under an exclusive license by AIP Publishing

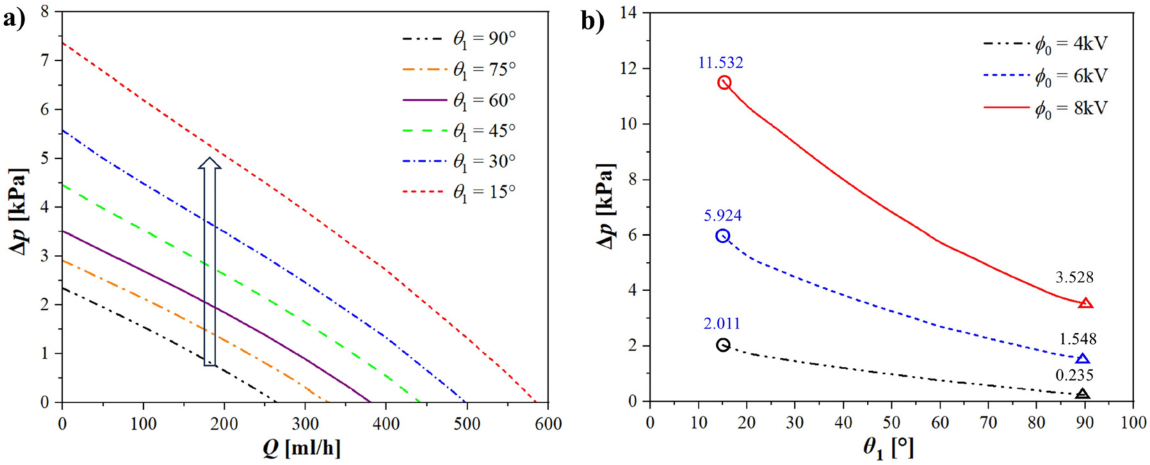

FIG. 15. Effect of θ_1 on (a) pressure difference–flow rate characteristic, for $\phi_0 = 6$kV, and (b) pressure difference as a function of θ_2, for $\theta_2 = 60°$ and Q = 100 ml/h.

and nonlinear) can be employed. Finally, the maximum efficiency reaches up to 10%. Although this efficiency seems to still be low compared with that of a traditional pump, it demonstrates that the VD-ECF micropump can operate more effectively with lower losses compared to any other ECF micropumps reported in previous studies. Therefore, this is to help improve the electrode-hydraulic efficiency of an ECF micropump, which is essentially very low. Moreover, the result obtained is to help reduce energy consumption and increase the operational lifespan of a VD-ECF micropump.

Based on the results obtained above, it was concluded that the applied voltage and channel configuration, including the trailing-edge emitter angle (θ_1) and the collector angle (θ_2), significantly affect the characteristics curves of the VD-ECF micropump. When the applied voltage increases, pressure difference (Δp), flow rate (Q), and maximum efficiency ($\eta_{\max}$) rise dramatically.[20] Additionally, the Δp-Q and $\eta_{\max}$-Q characteristic curves increase as θ_1 decreases from 90° to 15°. The maximum deviation obtained for the three values of Δp, Q, and $\eta_{\max}$ is 752.6%, 125.1%, and 200%, respectively (Figs. 15 and 16). Similarly, the Δp-Q characteristic curves lift when θ_2 decreases from 90° to 30°. The maximum deviations of Δp and Q for θ_2 of 90° and 15° are 52.3% and 26.7%, respectively (Fig. 6). Moreover, the overall electro-hydraulic efficiency was also affected by changing θ_2, as shown in Fig. 11.

Compared to previous ECF micropumps, the VD-ECF micropump demonstrates significantly superior performance. Specifically for the emitter, the pressure difference and efficiency increased by 65.1% and 45.8%, respectively, compared to conventional ones (Fig. 12). Moreover, this study achieved a maximum efficiency of up to 10%, as mentioned previously. On the other hand, previous studies frequently reported lower maximum efficiencies, for instance, 3.2% from Ueon's study[16] and 5% from Yanada's study.[41] For the collector, although the Venturi-shaped electrode with the θ_2 reduction seems not to improve overall efficiency, it enables the micropump to operate effectively across a broader range of pressure differences and flow rates at the same applied voltage. These results indicate that the VD-ECF micropump offers several advantages over previous designs, including a

01 October 2024 08:38:07

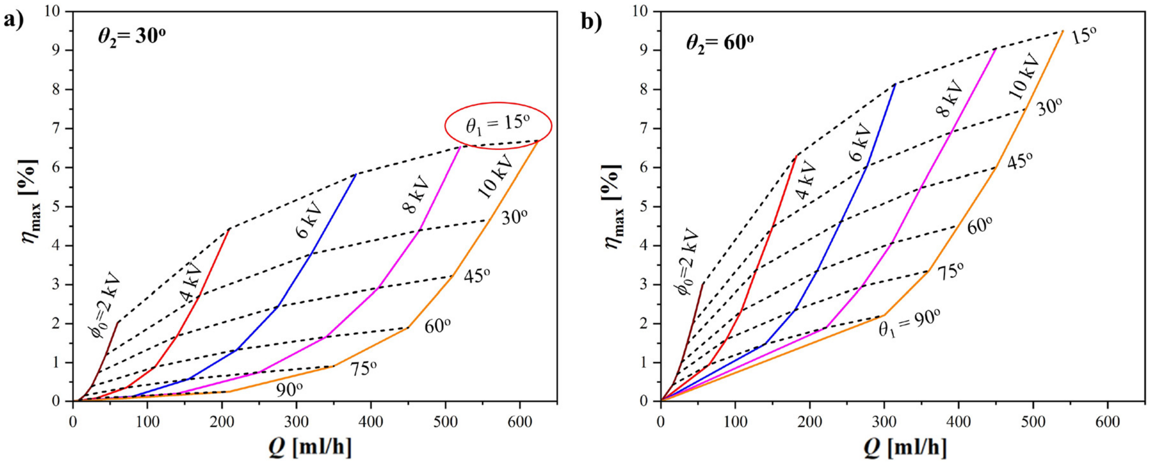

FIG. 16. The performance characteristic curves of VD-ECF micropump for various θ_1 and ϕ_0 (a) $\theta_2 = 30°$ and (b) $\theta_2 = 60°$.

Published under an exclusive license by AIP Publishing

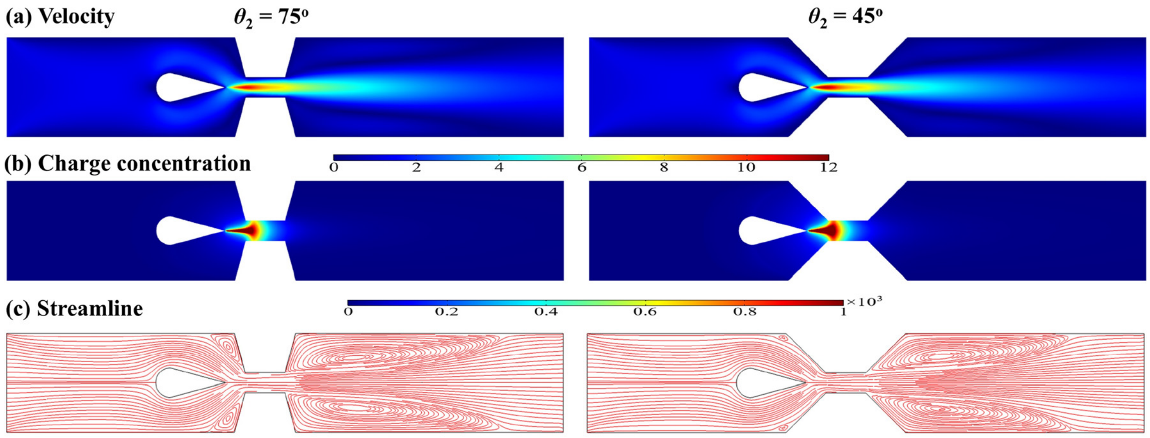

FIG. 17. Distribution of (a) velocity field, (b) charge concentration field, and (c) streamline for two particular θ_2 cases, for $\theta_1 = 30°$, $\phi_0 = 6$ kV, and $Q = 400$ ml/h.

flexible design with customizable teardrop and Venturi-shaped configurations for extending the operating performance. It also demonstrates high efficiency or lower energy consumption compared to the previous ECF micropumps.

Moreover, some guidelines for the design and manufacturing of ECF micropumps can be provided. In more detail, the overall electro-hydraulic efficiency is enhanced significantly by using the teardrop-shaped emitters instead of the conventional ones. Notably,

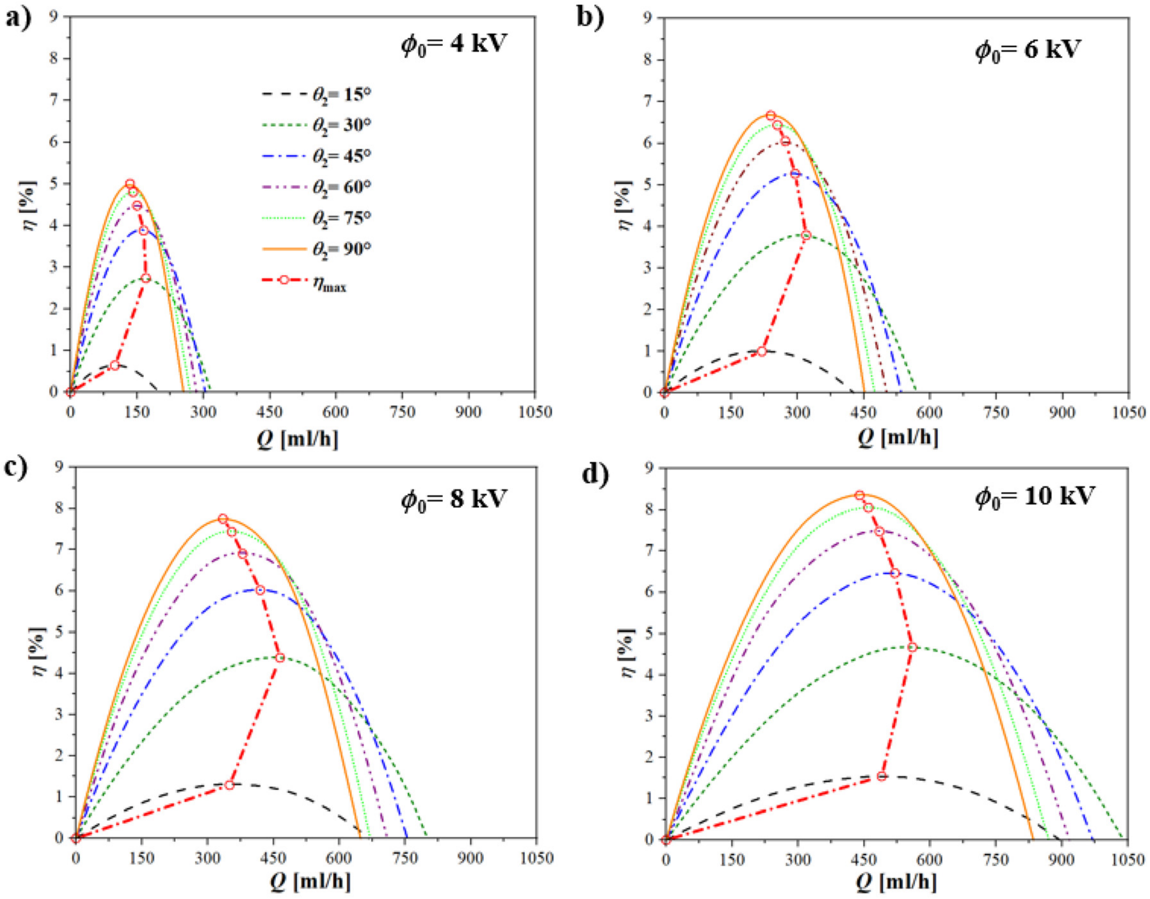

FIG. 18. Efficiency–flow rate characteristics curve for various values of θ_2 (a) $\phi_0 = 4$ kV, (b) $\phi_0 = 6$ kV, (c) $\phi_0 = 6$ kV, and (d) $\phi_0 = 10$ kV, for $\theta_1 = 30°$.

01 October 2024 08:38:07

Published under an exclusive license by AIP Publishing

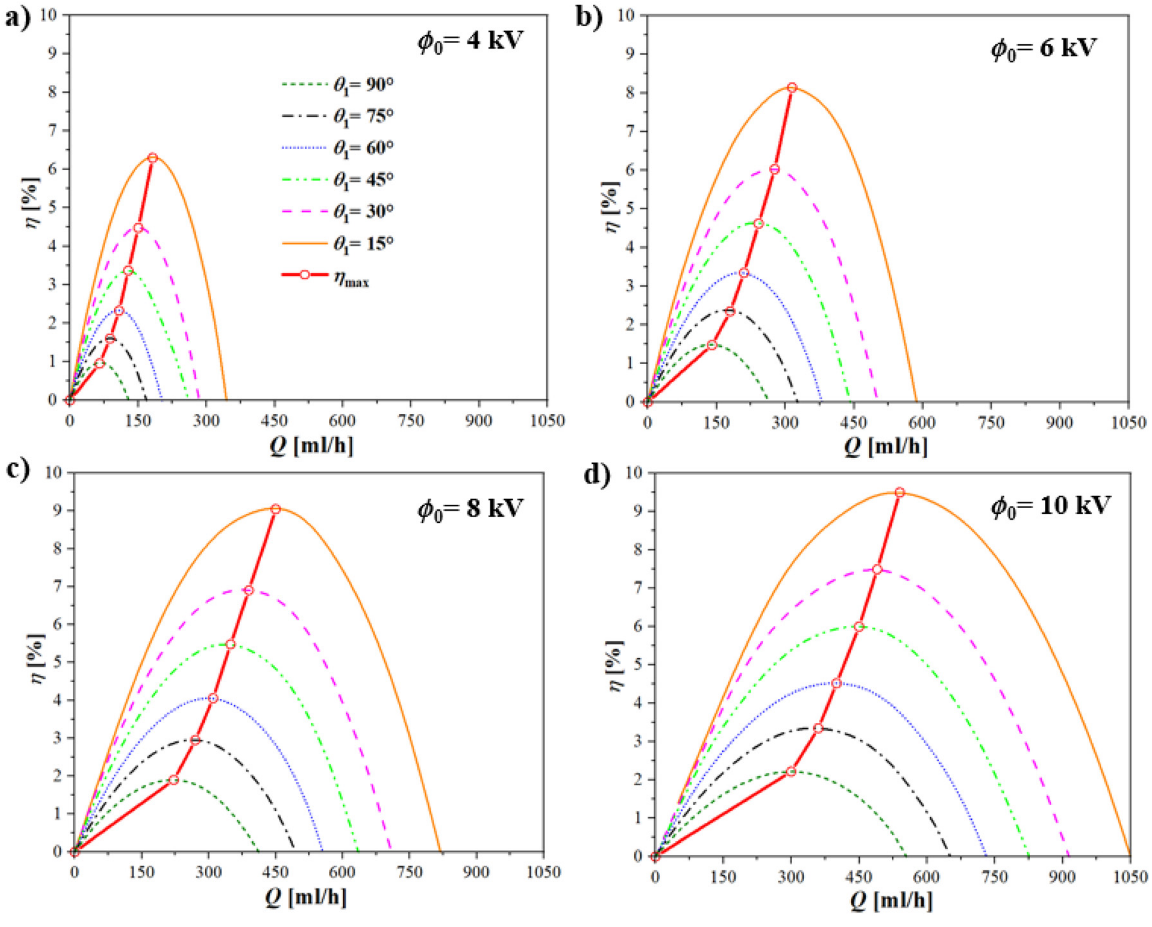

FIG. 19. Efficiency–flow rate characteristics curve for various values of θ_1 (a) $\phi_0 = 4$ kV, (b) $\phi_0 =$ 6 kV, (c) $\phi_0 = 6$ kV, and (d) $\phi_0 = 10$ kV, for $\theta_2 = 60°$.

01 October 2024 08:38:07

the trailing-edge emitter angle should be designed to be sufficiently small to ensure a feasible fabrication process. Moreover, the operating range of pressure difference and flow rate can be extended remarkably by designing the collector angles of less than 90°. The optimum value of this angle ranges from 25° to 30°, as mentioned previously. Additionally, since the electrode sizes are frequently very small, fabrication materials of electrodes with good electrical conductivity and less susceptible deformation should be used in high-applied voltage environments. This ensures that the electrodes maintain high performance and durability during micropump operation.

In summary, the VD-ECF micropump can be used or integrated into potential applications in microelectronics and biomedicine fields. Due to its precise control over fluid dynamics and enhanced efficiency, the VD-ECF micropump can be integrated into a micro-liquid cooling system for effective thermal management.[5] Its small size makes it ideal for micro-electronic devices where traditional cooling components are impractical. In laboratory-on-a-chip applications,[42] it can be used as a micro-hydraulic source.[12] Moreover, in microdialysis applications, the VD-ECF micropump can facilitate dialysate movement through microdialysis probes, enhancing the accuracy of sampling interstitial fluid for biochemical analysis. Other biomedical applications, including cell culturing, blood transport, and drug delivery, can be found in Wang and Fu's review study.[4]

IV. CONCLUSIONS

The dynamic behavior and electro-hydraulic performance of a new design ECF micropump with the Venturi-shaped collector and teardrop-shaped emitter have been investigated. The finite element method (FEM), in combination with the electrostatic and transport of species and Navier–Stokes equations, was used to model the electrokinetic flow in this study. The effect of various geometry parameters has been considered. Consequently, the majority results of this study are as follows:

(1) The numerical model is first proposed, and the numerical results show good agreement with both experimental data and numerical results reported in previous studies. Furthermore, the new design of the VD-ECF micropump with the Venturi-shaped collector and teardrop-shaped emitter has been first proposed.
(2) The effect of θ_1 and θ_2 on the flow behaviors in an ECF micropump is first explained from a physical viewpoint. This provides

Published under an exclusive license by AIP Publishing

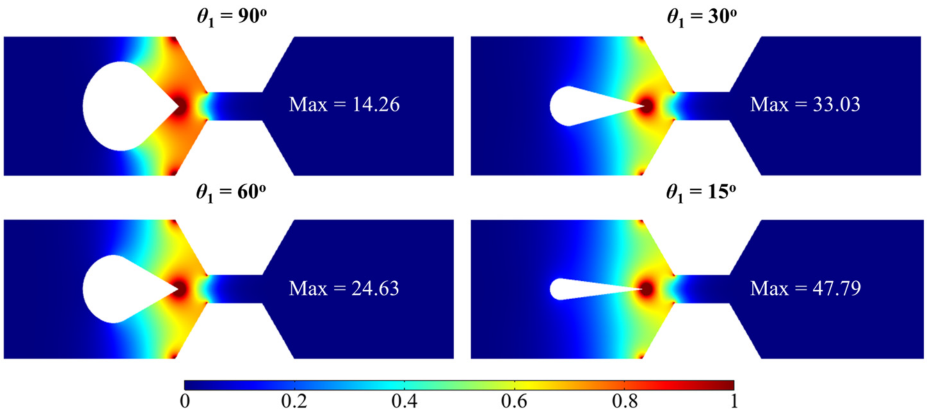

FIG. 20. Distribution of electric field for various values of θ_1 for $\theta_2 = 60°$ and $\phi_0 = 4$ kV.

a clear insight into the mechanism of the ECF micropump, which is challenging to find experimentally.

(3) The performance characteristic curves are elaborately constructed for various operating conditions of applied voltage and electrode angles. These diagrams play an important role in giving data on designing parameters for engineers.
(4) The operating ranges of pressure difference and flow rate of the VD-ECF micropump are extended remarkably, and they reach the maximum at θ_2 approximately from 25° to 30°. Since each operating condition requires a different output pressure and flow rate, it is useful to utilize a general-purpose micropump to meet all objectives.
(5) The maximum efficiency reaches nearly 10%, which is the highest efficiency value for various practical operating conditions. This ECF micropump can work as a micro-hydraulic power source for various fields of micro-actuation, cooling, and other potential engineering applications.

The results obtained from this study provide good guidelines and suggestions for the operation processes of the ECF micropump. In addition, this new micropump's design development and optimization could be utilized to enhance the performance applicability and accurate control of the ECF micropump that can be applied to microelectronics and biomedicine fields.

ACKNOWLEDGMENTS

This research is funded by the Vietnam National Foundation for Science and Technology Development (NAFOSTED) under Grant No. 107.03-2021.37.

AUTHOR DECLARATIONS

Conflict of Interest

The authors have no conflicts to disclose.

Author Contributions

The Khanh Lai: Data curation (equal); Formal analysis (equal); Investigation (equal); Methodology (equal); Writing – original draft (equal). **Toan Dinh:** Investigation (equal); Validation (equal); Visualization (equal); Writing – review & editing (equal). **Minh Duc Nguyen:** Data curation (equal); Formal analysis (equal); Methodology (equal); Software (equal). **Ich Long Ngo:** Conceptualization (equal); Formal analysis (equal); Funding acquisition (equal); Investigation (equal); Methodology (equal); Project administration (equal); Supervision (equal); Validation (equal); Writing – review & editing (equal).

DATA AVAILABILITY

The data that support the findings of this study are available from the corresponding author upon reasonable request.

REFERENCES

[1] S. Mi, H. Pu, S. Xia, and W. Sun, "A minimized valveless electromagnetic micropump for microfluidic actuation on organ chips," Sens. Actuators A: Phys. **301**, 111704 (2020).
[2] C. K. Byun, K. Abi-Samra, Y. K. Cho, and S. Takayama, "Pumps for microfluidic cell culture," Electrophoresis **35**, 245 (2014).
[3] M. Sedky, A. Ali, M. Abdel-Mottaleb, and M. Serry, "A new rapid-release SMA-activated micropump with incorporated microneedle arrays and polymeric nanoparticles for optimized transdermal drug delivery," Sens. Actuators B: Chem. **408**, 135549 (2024).
[4] Y.-N. Wang and L.-M. Fu, "Micropumps and biomedical applications—A review," Microelectron. Eng. **195**, 121 (2018).
[5] X.-L. Gao, X.-D. Bao, S.-J. Pang, J. Wu, K. Luo, and H.-L. Yi, "The electrohydrodynamic enhancement of heat transfer on interdigitated electrodes by a charge injection pump," Phys. Fluids **36**, 033612 (2024).
[6] P. K. Das and A. B. M. T. Hasan, *Mechanical Micropumps and Their Applications: A Review* (AIP Conference Proceedings, 2017).
[7] X. Luo, L. Yang, and Y. Cui, "Micropumps: Mechanisms, fabrication, and biomedical applications," Sens. Actuators A: Phys. **363**, 114732 (2023).
[8] J.-w. Kim, T. Suzuki, S. Yokota, and K. Edamura, "Tube-type micropump by using electro-conjugated fluid (ECF)," Sens. Actuators A: Phys. **174**, 155 (2012).
[9] Y. Kuroboshi, K. Takemura, and K. Edamura, "Understanding of electro-conjugate fluid flow with dibutyl decanedioate using numerical simulation—Calculating ion mobility using molecular dynamics simulation," Sens. Actuators B: Chem. **255**, 448 (2018).
[10] Y. Abe, K. Takemura, K. Sato, S. Yokota, and K. Edamura, "Droplet μTAS using electro-conjugate fluid—Feedback position control of multiple droplets in flow channel matrix," Sens. Actuators A: Phys. **198**, 1 (2013).
[11] Z. Mao, K. Yoshida, and J.-w. Kim, "Developing O/O (oil-in-oil) droplet generators on a chip by using ECF (electro-conjugate fluid) micropumps," Sens. Actuators B: Chem. **296**, 126669 (2019).
[12] S. Yokota, A. Sadamoto, Y. Kondoh, Y. Otsubo, and K. Edamura, "A micro motor using electroconjugate fluids (ECFs)," JSME Int. J. Ser. C **44**, 756 (2001).
[13] F. Abhari, H. Jaafar, and N. A. M. Yunus, "A comprehensive study of micropumps technologies," Int. J. Electrochem. Sci. **7**, 9765 (2012).

01 October 2024 08:38:07

Published under an exclusive license by AIP Publishing

[14]K. Takemura, S. Yokota, and K. Edamura, "Development and control of a micro artificial muscle cell using electro-conjugate fluid," Sens. Actuators A: Phys. **133**, 493 (2007).

[15]K. Mori, A. Yamaguchi, K. Takemura, S. Yokota, and K. Edamura, "Control of a novel flexible finger using electro-conjugate fluid with built-in angle sensor," Sens. Actuators A: Phys. **183**, 75 (2012).

[16]S. Ueno, K. Takemura, S. Yokota, and K. Edamura, "Micro inchworm robot using electro-conjugate fluid," Sens. Actuators A: Phys. **216**, 36 (2014).

[17]K. Takemura, S. Yokota, M. Suzuki, K. Edamura, H. Kumagai, and T. Imamura, "A liquid rate gyroscope using electro-conjugate fluid," Sens. Actuators A: Phys. **149**, 173 (2009).

[18]S. Yokota, W. S. Seo, K. Yoshida, and K. Edamura, "A thin-planar pump using electro-conjugate fluid (ECF) for liquid cooling of electronic chips," Trans. Jpn. Soc. Mech. Eng. C **71**(709), 2798–2804 (2005).

[19]L. Cao, S. Mantell, and D. Polla, "Design and simulation of an implantable medical drug delivery system using microelectromechanical systems technology," Sens. Actuators A: Phys. **94**, 117 (2001).

[20]D. Han, H. Wang, S. Yokota, and J.-W. Kim, "Configurations of triangular prism and slit electrode pairs to enhance the performance of electro-conjugate fluid micropumps," J. Micromech. Microeng. **30**, 025007 (2020).

[21]Y. Kuroboshi, K. Takemura, and K. Edamura, "Efficient electrode configuration for electro-conjugate fluid flow generation with dibutyl decanedioate: Experimental and theoretical investigation," Sens. Actuators A: Phys. **279**, 223 (2018).

[22]I. L. Ngo, T. K. Lai, H. J. Choi, H. T. T. Le, G. M. Kim, and T. D. Dang, "A study on mixing performance of dean flows through spiral micro-channel under various effects," Phys. Fluids **32**, 022004 (2020).

[23]K. Mori, H. Yamamoto, K. Takemura, S. Yokota, and K. Edamura, "Dominant factors inducing electro-conjugate fluid flow," Sens. Actuators A: Phys. **167**, 84 (2011).

[24]Y. Iijima, K. Hosoda, K. Takemura, K. Fukagata, and K. Edamura, "Numerical simulation of electro-conjugate fluid flow considering electric double layer," Mech. Eng. J. **2**, 15-00341 (2015).

[25]J.-w. Kim, Y. Tanabe, and S. Yokota, "Comprehending electro-conjugate fluid (ECF) jets by using the Onsager effect," Sens. Actuators A: Phys. **295**, 266 (2019).

[26]R. Abe, K. Takemura, K. Edamura, and S. Yokota, "Concept of a micro finger using electro-conjugate fluid and fabrication of a large model prototype," Sens. Actuators A: Phys. **136**, 629 (2007).

[27]H. Yamamoto, K. Mori, K. Takemura, L. Yeo, J. Friend, S. Yokota, and K. Edamura, "Numerical modeling of electro-conjugate fluid flows," Sens. Actuators A: Phys. **161**, 152 (2010).

[28]T. Matsubara, H. H. Huynh, K. Yoshida, and J.-w. Kim, "Development of MEMS-fabricated bidirectional ECF (electro-conjugate fluid) micropumps," Sens. Actuators A: Phys. **295**, 317 (2019).

[29]J.-w. Kim, Y. Yamada, and S. Yokota, "Micro ECF (electro-conjugate fluid) hydraulic power sources based on the modular design of TPSEs (triangular prism and slit electrode pairs)," Int. J. Adv. Manuf. Technol. **106**, 627 (2019).

[30]A. Manz, C. S. Effenhauser, N. Burggraf, D. J. Harrison, K. Seiler, and K. Fluri, "Electroosmotic pumping and electrophoretic separations for miniaturized chemical analysis systems," J. Micromech. Microeng. **4**, 257 (1994).

[31]K. D. Tran, Y. Kojima, and H. Yanada, "Measurement and numerical simulation of flow and electric fields in charge injection type of electrostatic oil filter," JFPS Int. J. Fluid Power Syst. **2**, 1 (2009).

[32]H. Yanada, T. Yamada, Y. Asai, and Y. Terashita, "Measurement and numerical simulation of ion drag pump characteristics," J. Fluid Sci. Technol. **5**, 617 (2010).

[33]M. Nishikawara, M. Shimada, M. Saigo, and H. Yanada, "Numerical investigation of the characteristics of an ion drag pump," J. Electrost. **84**, 23 (2016).

[34]T. K. Lai, K. D. Tran, and I. L. Ngo, *A Numerical Study on the Thermo-Electrohydrodynamic Performance of ECF Micro-Pumps* (Springer, Hanoi, Vietnam, 2024).

[35]F. M. White, *Fluid Mechanics*, 4th ed. (McGraw Hill Publishing Company Ltd., 2001).

[36]Y. A. Çengel and J. M. Cimbala, *Fluid Mechanics: Fundamentals and Applications* (McGraw-Hill Higher Education, 2010).

[37]I. Kano and T. Nishina, "Effect of electrode arrangements on EHD conduction pumping," IEEE Trans. Ind. Appl. **49**, 679 (2013).

[38]Y. Peng, D. Li, X. Yang, Z. Ma, and Z. Mao, "A review on electrohydrodynamic (EHD) pump," Micromachines **14**, 321 (2023).

[39]D. Han, H. Gu, J.-w. Kim, and S. Yokota, "A bio-inspired 3D-printed hybrid finger with integrated ECF (electro-conjugate fluid) micropumps," Sens. Actuators A: Phys. **257**, 47 (2017).

[40]H. Soğukpinar, "Numerical simulation of 4-digit inclined naca 00xx airfoils to find optimum angle of attack for airplane wing," Uludag Univ. J. Faculty Eng. **22**, 169 (2017).

[41]H. Yanada, S. Hakama, T. Miyashita, and N. Zhang, "An investigation of an ion drag pump using a needle–mesh electrode configuration," Proc. Inst. Mech. Eng., C: J. Mech. Eng. Sci. **216**, 325 (2002).

[42]T. T. Nguyen, M. Pham, and N. S. Goo, "Development of a peristaltic micropump for bio-medical applications based on mini LIPCA," J. Bionic Eng. **5**, 135 (2008).

01 October 2024 08:38:07

Published under an exclusive license by AIP Publishing